Title: Photon recycling in Lead-Iodide Perovskite Solar Cells

Authors: Luis M. Pazos-Outón[1], Monika Szumilo[1], Robin Lambol[1], Johannes M. Richter[1], Micaela Crespo-Quesada[2], Mojtaba Abdi-Jalebi[1], Harry J. Beeson[1], Milan Vrucinic[1], Mejd Alsari[1], Henry J. Snaith[4], Bruno Ehrler[3], Richard H. Friend[1,*] and Felix Deschler[1,*].

Affiliations:

[1]Cavendish Laboratory, University of Cambridge, JJ Thomson Avenue, CB3 0HE, Cambridge, UK

[2]Department of Chemistry, University of Cambridge, CB2 1EW, Cambridge, UK.

[3]FOM Institute AMOLF, Center for Nanophotonics, Science Park 104, 1098 XG Amsterdam, The Netherlands.

[4]Clarendon Laboratory, Department of Physics, University of Oxford, OX1 3PU, Oxford, UK.

*Correspondence to: rhf10@cam.ac.uk and fd297@cam.ac.uk

Abstract: Lead-halide perovskites have emerged as high-performance photovoltaic materials and present a promising candidate for thin film photovoltaic applications. We map the propagation of photogenerated luminescence and charges away from a local photoexcitation spot in thin films of lead tri-iodide perovskites, and observe light emission at distances of 50 μm and beyond. Over these distances, the peak of the internal photon spectrum red-shifts from 765 nm to ≥800 nm. Using a lateral-contact solar cell with selective electron- and hole-collecting contacts charge extraction for photoexcitation at distances over 50 μm away from the contacts is observed. We show that these large transport distances arise from repeated recycling between photons and electron-hole pairs. Energy transport in these perovskites is therefore not limited by diffusive charge transport, but can occur over long distances through multiple absorption-diffusion-emission events. This process creates high excitation densities within the active perovskite layer, and, as with GaAs solar cells, allows high open circuit voltages.

Keywords: Photon recycling, lead-halide perovskites, long-range energy transfer, back-contact solar cell

One Sentence Summary: We demonstrate photon recycling in lead iodide perovskite solar cells, which allows for high long charge extraction lengths through multiple absorption-emission events, and contributes to the exceptionally high reported open circuit voltages.

Main Text:

Hybrid lead halide perovskite photovoltaics have shown an exceptional rise in power conversion efficiency since their original publication (*1*) to efficiencies which are almost comparable to crystalline silicon (*2–7*). This excellent photovoltaic performance has been attributed to well-suited material properties such as high absorption cross-sections (*8*), long charge carrier lifetimes (*9*) and high emission yields (*10*). Recent studies in single crystals have reported charge diffusion lengths of 175 μm (*11, 12*), and in polycrystalline thin films vertical diffusion lengths have been found to be longer than one micron (*13, 14*) . Together with high radiative recombination yields and long carrier lifetimes this raises the question if absorption and reemission of excited carriers can occur during the transport. We report here that such 'photon recycling' does indeed play a central role, allowing considerable increases over current descriptions in the characteristic lengths for charge and energy transport. This implies that some reinterpretation of the perovskite solar cell literature is therefore required.

Highly crystalline inorganic semiconductors with high internal quantum yields, such as GaAs, demonstrate the current record efficiencies in single junction solar cells (*15, 16*). The low non-radiative recombination rates, and high photoluminescence (PL) yields, of these materials allow one photoexcited state to undergo multiple radiative emission-absorption events before it is lost through non-radiative decay (*17, 18*). This photon recycling effect, together with photonic confinement due to the difference in refractive index between the active material and its surroundings, leads to a built-up of excited state population in the bulk of the material, similar to a solar concentration effect (*17*). Additionally, the length scales for energy transport are not limited to a single charge diffusion length, but can occur through multiple recombination-emission events in an interchange between light and charge states, which dramatically enhances the transport length scales.

Previous work on lead iodide perovskites has found a sharp absorption onset at the optical band-edge, with an Urbach Tail slope close to that of GaAs (*8, 19*), while the PL spectrum is homogeneously broadened by interaction with phonons, leading to a considerable intensity beyond the band-edge (*20*). Additionally, long carrier lifetimes and low non-radiative losses have been reported (*9, 10*). These are conditions that could support photon recycling.

We study thin perovskite films (details of preparation and characterisation in the SI) on glass substrates, with a thickness of ~100 nm. Under these conditions, only 10-15% of internally generated PL escapes to the air above or to the glass below (calculation in the SI), and remaining emission is guided within the film (*21*). We measure the spatial distribution of photo-generated emission using a confocal optical microscope setup with separately-controlled excitation and collection objectives and a spatial resolution of ~1.5 μm, see Figure 1A and Supporting Fig. S1. Photons propagating in the film can be scattered out of the film or be absorbed and re-emitted isotropically. We measure the emission from the edge of the film, allowing the detection of both components. These results provide a direct probe of the internal photon distribution traveling through the film. Figure 1B shows spatial emission mapping. When excitation is close to the edge ($\leq$ 4 μm), the observed spectrum is similar to the macroscopic PL of this film, centred around 765 nm (cf. Figure 1C). However, when the excitation objective is moved further away from the collection spot, the internal spectrum continuously red-shifts, beyond 800 nm after a separation of 50 μm. Unexpectedly, at these distances, we still detect a blue (765 nm) component in the spectrum at wavelengths similar to the initial emission spectrum, the origin of which we discuss below.

Absorption coefficients α_λ of the films are measured using photothermal deflection spectroscopy (PDS), and are compared with photoluminescence excitation spectrum (PLE) in Figure 1C. Under conditions where photons are mostly confined within a slab (formed here

by the glass/perovskite/air structure) the Beer-Lambert law gives a decay in spectral photon population I_λ away from a point-like excitation spot with radius r_0:

$$I_\lambda(r) = \frac{r_0}{r} I_{\lambda_0} . \mathrm{e}^{-(\alpha_\lambda \cdot r)} \quad (1)$$

This relation indicates that the decay is mono-exponential for each wavelength, with an additional radial factor. Using this equation the predicted spectral decay map following this law is plotted in Figure 1D. We find that the measured decay in the different spectral regions is significantly slower than the prediction from the Beer-Lambert law. To illustrate the difference, the decay for selected wavelengths is extracted in Figure 1E. Beer-Lambert predictions do not take scattering into account, which may further reduce the emission intensity, particularly in spectral regions of very low absorption.

We attribute the main, red-shifted peak to photons guided within the film. These are absorbed by the tail of the band-edge and generate electron-hole pairs far from the original excitation spot. The internal photon spectral distribution is biased towards longer wavelength photons since these travel further between emission and absorption events. When these recombine, they regenerate the original emission spectrum that peaks near 765 nm. We note that the photon energy gain between absorption and re-emission occurs via phonon-assisted thermalization.

With the observed spatial decay of photon intensity, charges are expected to be generated at comparable distances. To measure the spatial charge distribution directly, we designed a lateral solar cell with electron and hole selective electrodes. Figure 2A shows the fabrication process of this back-contacted device. It starts with a plain sheet of ITO covering a glass substrate. Photolithography is then used to make a pattern of ITO with interdigitated electrodes. The channel and electrode width is ~4 µm. This relates to a pitch distance, measured from the centre of each electrode, of 8 µm in total. Electrodeposition is employed

to selectively deposit electron- and hole-blocking layers. On half of the electrodes TiO_2 was deposited from a solution of $Ti(O_2)SO_4$, and poly-3,4-ethylenedioxythiophene (PEDOT) from an 3,4-ethylenedioxythiophene (EDOT) monomer-based solution is deposited in the remaining electrode surface. The TiO_2 layer is formed by hydrolysis, whilst the PEDOT film forms by polymerization under an external bias. Finally, a layer of perovskite is spincoated from a standard precursor solution based on methylammonium iodide mixed with lead acetate in DMF (*22*). (see experimental section in the SI for a full description).

The electric response of this device was measured in the dark and a diode-like rectifying behavior was found. Under solar irradiation a photovoltaic response of the device with an open-circuit voltage of 0.5 V was observed (Figure S14), showing effective carrier selectivity at the electrodes. Photocurrent extraction appears however to be limited compared to vertical solar cells, which we postulate to be due to energy barriers at the electrodes and an unfavorable charge collection geometry. For comparison, a lateral solar cell without selective layers is shown in the supplementary information (Figure S15), which shows a reduced charge selectivity, and very limited voltage and photocurrent.

We used a confocal microscope setup to map the spatially resolved photocurrent generation in these devices with an excitation resolution below 1 μm. The photocurrent then probes the number of photo-excited carriers which reach the electrodes. Figure 2B shows a spatial map of photocurrent both across the interdigitated electrodes (< 0 μm) and for photoexcitation beyond the electrodes (0 to 100 μm). The full operation of this 'back-bottom contact' solar cell will be reported elsewhere, but we draw attention to the very slow fall-off in photocurrent for excitation beyond the edge of the electrode structure, see also Figure 2C. This extends significantly beyond reported diffusion lengths of lead halide perovskite thin films.

In the range of excitation fluences used here, PL in perovskites is mainly due to bimolecular recombination of charge carriers with volume density *n*, i.e. $PL \propto n^2$, consistent with electron-hole recombination (*10*, *23*, *24*). Hence, we can relate the locally generated PL, taken around the PL emission peak (765 nm), with the local charge density, and $\sqrt{PL} \propto n$ is a probe of the spatial charge distribution. Since $\sqrt{PL}$ decays cylindrically, it has to be geometrically corrected by performing a line integral of $\sqrt{PL}$ over the length of the electrode, in order to compare it with the photocurrent measurements.

In Figure 2C we compare the decay of the integrated $\sqrt{PL}$ with the measured spatial decay of the photocurrent. We observe a very similar decay in photocurrent and integrated $\sqrt{PL}$ beyond 8 µm, which is the resolution set by the electrode geometry, The agreement between these two quantities indicates that the red-shifted component of the recycled photons allows excitation transport over long distances, beyond carrier diffusion lengths, which eventually can be extracted as photocurrent from a solar cell.

To model this, a system of cylindrically symmetric partial differential equations was set up and solved (full details in the SI):

$$\frac{dn}{dt} = D\nabla^2 n + G + \frac{c}{n_s}\sum_{\lambda} \alpha_\lambda \gamma_\lambda - k_1 n - k_2 n^2$$

$$\frac{d\gamma_\lambda}{dt} = D_\lambda \nabla^2 \gamma_\lambda - \frac{c}{n_s}\alpha_\lambda \gamma_\lambda + (k_2 n^2 P_{stay})P_\lambda$$

The charge carrier concentration $\boldsymbol{n}$ and the photon density $\boldsymbol{\gamma}$ were modeled (at different wavelengths λ) as a function of distance from the excitation spot. Input parameters are reported experimental values for carrier diffusion (diffusion constant D = 0.5cm^{2}s^{-1}, (*9*, *11*, *12*)), mono- and bimolecular recombination of carriers ($k_1 = 10^6$ s^{-1}, $k_2 = 10^{-10}$ cm^{3}s^{-1}, our own

measurements and (*10*, *25*)), and the measured wavelength-dependent absorption coefficients α_λ (cf. Figure 1C). We note that the experimentally measured external bimolecular rate has to be adjusted to take photon recycling into account (*26*, *27*). All absorption of photons is assumed to result in the creation of charge pairs, but only the bimolecular channel is radiative, with the spectrum as shown in Figure 1C, and a proportion 1-P_{stay} (modelled to be 12.5%, see the SI) of these are lost due to optical transmission out of the perovskite at the interfaces. The external photoluminescence quantum efficiency (PLQE) results from multiple internal recycling events and is related to the internal PLQE by the geometric series:

$$\mathrm{PLQE_{ext}} = \sum_{r=1}^{\infty} (\mathrm{PLQE_{int}})^r (1 - P_{escape})^{r-1} P_{escape} = \frac{\mathrm{PLQE_{int}} P_{escape}}{1 - \mathrm{PLQE_{int}}(1 - P_{escape})} \quad (2)$$

The external PLQE varies with distance from the excitation spot and carrier density (Figure 3A). We find that photon recycling can be very efficient close to the excitation spot, but drops off at larger distances where charge carrier densities are smaller. From Eq. 2 we find that internal PLQEs can exceed 50% for 1-sun illumination (internal carrier density~10^{15} cm^{-3}), which correspond to lower measured external PLQEs of ~10%. We note that the observed recycling effect on extraction would be increased in a solar cell with homogenous illumination, which gives constant carrier densities over the full active area.

Using this model to match the experimental photocurrent, it is clear that recycling has to be taken into account to explain the observed long spatial decays (Figure 3B). The model predicts on average one recycling event per photoexcited charge carrier under 1-sun illumination before the carrier decays non-radiatively (calculation in the SI) in a perovskite film in air on glass. This value relates to a photon recycling-assisted average excitation travel distance of 20 μm (Figure S18). We also find that the average travel distance can be enhanced at larger charge densities (for example under high fluences) and can reach values beyond 50 μm.

These results demonstrate that externally measured photoluminescence in lead-halide perovskites can result from several recycling events. In terms of electron-hole transport, the results suggest that the average distance a charge carrier can travel in these materials is not limited by the charge carrier diffusion length, for as long as recombination is radiative and the photon stays in the film, the electron-hole pair can be regenerated and propagate over large distances. This creates a distinction between extraction and charge diffusion lengths, and solves the existing contradiction of reported high recombination rates and long 'diffusion' lengths in the literature.

What are the implications of the observations presented here for standard thin-film perovskite solar cells (*6, 28*)? The thin film samples used in our work provide useful model systems for these structures. Using the model and parameters developed above, we estimate that, under open-circuit conditions, in a device with a thickness of 350 nm and non-quenching electrodes, recycling produces a doubling of the internal photon density under 1 sun illumination. These effects can be enhanced even further by minimizing non-radiative decay channels and under higher fluences, such as in solar concentrators, where high bimolecular recombination rates dominate. In the ideal case of unity PLQE and perfect back mirror, photon recycling can produce internal photon densities up to 25 suns ($4n^2$ with n = 2.5) (*29*) in perovskite solar cells at open circuit. This indicates that photon management, such as the use of highly reflective back mirrors to minimize photonic losses and texturing of the top surface, are promising approaches to utilize photon recycling to improve photo-conversion efficiencies of perovskite solar cells towards the Shockley-Queisser limit. Higher photon densities lead to higher internal luminescence and to a build-up of excited charges, which increase the split of quasi-Fermi levels and enhance the achievable open circuit voltage in a solar cell.

References:

1. A. Kojima, K. Teshima, Y. Shirai, T. Miyasaka, Organometal Halide Perovskites as Visible-Light Sensitizers for Photovoltaic Cells. *J. Am. Chem. Soc.* **131**, 6050–6051 (2009).
2. J.-H. Im, C.-R. Lee, J.-W. Lee, S.-W. Park, N.-G. Park, 6.5% Efficient Perovskite Quantum-Dot-Sensitized Solar Cell. *Nanoscale*. **3**, 4088 (2011).
3. M. M. Lee, J. Teuscher, T. Miyasaka, T. N. Murakami, H. J. Snaith, Efficient Hybrid Solar Cells Based on Meso-Superstructured Organometal Halide Perovskite. *Science (80-.).* **338**, 643–647 (2012).
4. M. Liu, M. B. Johnston, H. J. Snaith, Efficient planar heterojunction perovskite solar cells by vapour deposition. *Nature*. **501**, 395–8 (2013).
5. H.-S. Kim *et al.*, Lead iodide perovskite sensitized all-solid-state submicron thin film mesoscopic solar cell with efficiency exceeding 9%. *Sci. Rep.* **2**, 591 (2012).
6. N. J. Jeon *et al.*, Compositional engineering of perovskite materials for high-performance solar cells. *Nature*. **517**, 476–480 (2015).
7. J. Burschka *et al.*, Sequential deposition as a route to high-performance perovskite-sensitized solar cells. *Nature*. **499**, 316–9 (2013).
8. S. De Wolf *et al.*, Organometallic halide perovskites: Sharp optical absorption edge and its relation to photovoltaic performance. *J. Phys. Chem. Lett.* **5**, 1035–1039 (2014).
9. C. Wehrenfennig, G. E. Eperon, M. B. Johnston, H. J. Snaith, L. M. Herz, High charge carrier mobilities and lifetimes in organolead trihalide perovskites. *Adv. Mater.* **26**, 1584–1589 (2014).
10. F. Deschler *et al.*, High Photoluminescence Efficiency and Optically Pumped Lasing in Solution-Processed Mixed Halide Perovskite Semiconductors. *J. Phys. Chem. Lett.* **5**, 1421–1426 (2014).
11. Q. Dong *et al.*, Electron-hole diffusion lengths > 175 m in solution-grown CH3NH3PbI3 single crystals. *Science (80-.).* **347**, 967–970 (2015).
12. D. Shi *et al.*, Low trap-state density and long carrier diffusion in organolead trihalide perovskite single crystals. *Science (80-.).* **347**, 519–522 (2015).
13. G. Xing *et al.*, Long-Range Balanced Electron- and Hole-Transport Lengths in Organic-Inorganic CH3NH3PbI3. *Science (80-.).* **342**, 344–347 (2013).
14. S. D. Stranks *et al.*, Electron-Hole Diffusion Lengths Exceeding 1 Micrometer in an Organometal Trihalide Perovskite Absorber. *Science (80-.).* **342**, 341–344 (2013).
15. E. Yablonovitch, O. D. Miller, S. R. Kurtz, in *Conference Record of the IEEE Photovoltaic Specialists Conference* (IEEE, 2012), vol. 3, pp. 1556–1559.
16. L. S. Mattos *et al.*, in *Conference Record of the IEEE Photovoltaic Specialists Conference* (IEEE, 2012), pp. 3187–3190.
17. O. D. Miller, E. Yablonovitch, S. R. Kurtz, Strong internal and external luminescence as solar cells approach the Shockley-Queisser limit. *IEEE J. Photovoltaics*. **2**, 303–311 (2012).

18. E. Dupont, H. C. Liu, M. Buchanan, S. Chiu, M. Gao, Efficient GaAs light-emitting diodes by photon recycling. *Appl. Phys. Lett.* **76**, 4 (2000).

19. A. Sadhanala *et al.*, Preparation of Single-Phase Films of $CH_3NH_3Pb(I_{1-x}Br_x)_3$ with Sharp Optical Band Edges. *J. Phys. Chem. Lett.* **5**, 2501–2505 (2014).

20. C. Wehrenfennig, M. Liu, H. J. Snaith, M. B. Johnston, L. M. Herz, Homogeneous Emission Line Broadening in the Organo Lead Halide Perovskite $CH_3NH_3PbI_{3-x}Cl_x$. *J. Phys. Chem. Lett.* **5**, 1300–1306 (2014).

21. I. Suárez, E. J. Juárez-Pérez, J. Bisquert, I. Mora-Seró, J. P. Martínez-Pastor, *Adv. Mater.*, in press, doi:10.1002/adma.201503245.

22. W. Zhang *et al.*, Ultrasmooth organic-inorganic perovskite thin-film formation and crystallization for efficient planar heterojunction solar cells. *Nat Commun.* **6**, 6142 (2015).

23. Y. Yamada, T. Nakamura, M. Endo, A. Wakamiya, Y. Kanemitsu, Photocarrier Recombination Dynamics in Perovskite $CH_3NH_3PbI_3$ for Solar Cell Applications. *J. Am. Chem. Soc.* **136**, 11610–11613 (2014).

24. L. M. Herz, Charge Carrier Dynamics in Organic-Inorganic Metal Halide Perovskites. *arXiv*, 1–26 (2014).

25. M. B. Johnston, L. M. Herz, Hybrid Perovskites for Photovoltaics: Charge-Carrier Recombination, Diffusion, and Radiative Efficiencies. *Acc. Chem. Res.* **in press** (2015), doi:10.1021/acs.accounts.5b00411.

26. R. K. Ahrenkiel *et al.*, Ultralong minority- carrier lifetime epitaxial GaAs by photon recycling. *Appl. Phys. Lett.* **55**, 1088–1090 (1989).

27. P. Renaud, F. Raymond, B. Bensaïd, C. Vèrié, Influence of photon recycling on lifetime and diffusion coefficient in GaAs. *J. Appl. Phys.* **71**, 1907 (1992).

28. M. M. Lee, J. Teuscher, T. Miyasaka, T. N. Murakami, H. J. Snaith, Efficient Hybrid Solar Cells Based on Meso-Superstructured Organometal Halide Perovskites. *Science (80-.).* **338**, 643–647 (2012).

29. Q. Lin *et al.*, Electro-optics of perovskite solar cells. *Nat. Photonics*. **9**, 106–112 (2014).

Acknowledgments: The authors acknowledge financial support from the Engineering and Physical Sciences Research Council of the UK (EPSRC) and King Abdulaziz City for Science and Technology (KACST). L.M.P.O. and H.J.B. also thank the Nano doctoral training center (NanoDTC) for financial support. M.S., M.V. and J.M.R. thank the Winton programme for the physics of sustainability. M.C.Q would like to thank the Marie Curie Actions (FP7-PEOPLE-IEF2013) for funding. M.A.J. thanks Nyak Technology Ltd for PhD scholarship and B.E. acknowledges the Foundation for Fundamental Research on Matter (FOM), which is part of the Netherlands Organization for Scientific Research (NWO). F.D. acknowledges funding through a Herchel Smith Research Fellowship. We acknowledge Prof. Henning Sirringhaus, Prof. Neil Greenham, Prof. Ullrich Steiner, Dr. Erwin Reisner and Prof. Richard Phillips for providing financial support and access to their facilities.

Author contributions: L.M.P.O., F.D. and R.H.F conceived the experiment. L.M.P.O. conceived the device fabrication route with contributions from M.S. and B.E., coordinated device fabrication and characterization, and performed data analysis. M.S. developed and performed photolithography of ITO, performed confocal microscope measurements with contributions from F.D. and M.V., and analysed data. R.L. created and implemented the modelling with contributions from J.R. and L.M.P.O. J.R. performed transient photoluminescence measurements. M.C.Q. developed and performed TiO2 electrodeposition. H.B. developed and performed PEDOT electrodeposition. M.A.A. optimised device fabrication. M.A.J. performed photothermal deflection spectroscopy measurements, perovskite film deposition and characterization. H.J.S. gave useful insights for data interpretation. L.M.P.O., F.D. and R.H.F wrote the manuscript with contributions from all authors.

Figures:

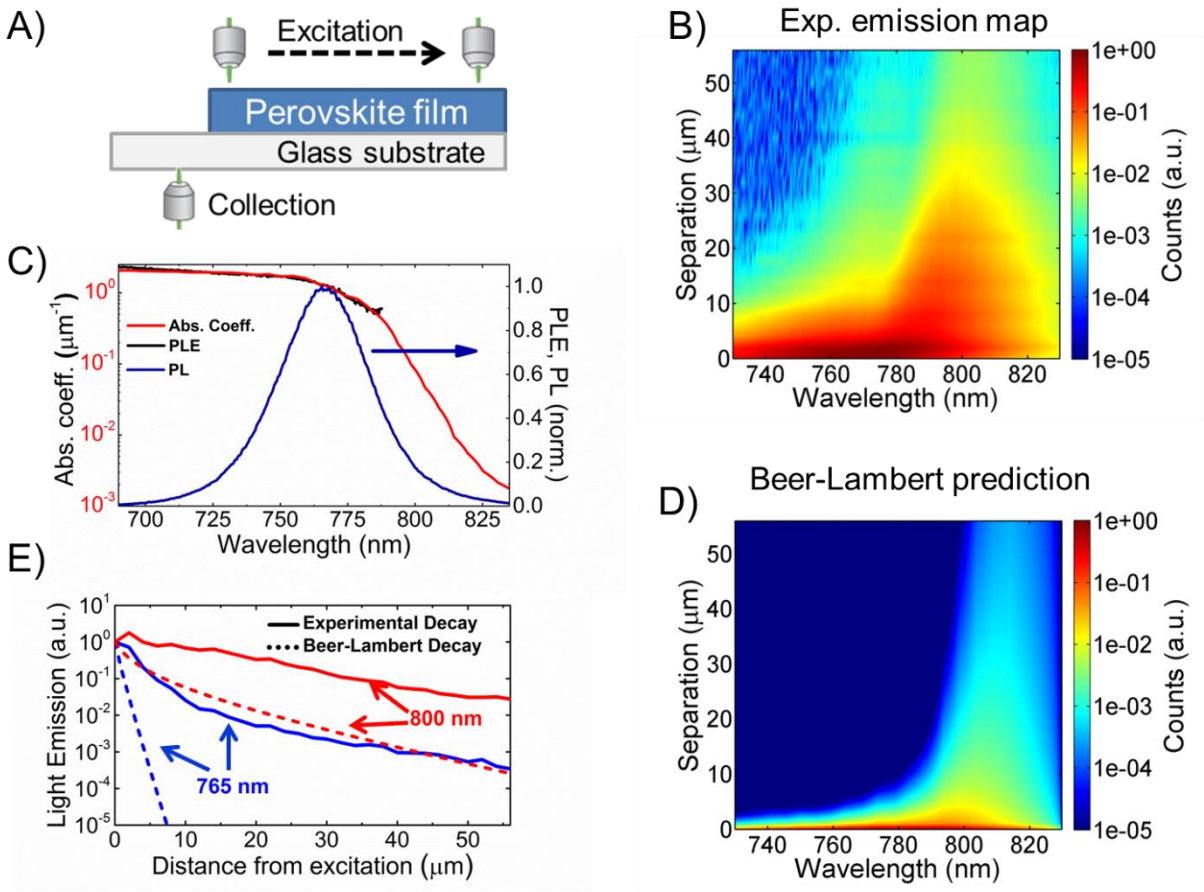

Fig. 1. Spatial mapping of emission and photon spectrum A) Graphical representation of microscope setup and measurement geometry. B) Experimentally measured light emission map for different separation distances between excitation and collection. C) Comparison of PL with PL emission (PLE) and photothermal deflection spectra (PDS). D) Predicted spatial light emission spectra from cylindrically decaying Beer-Lambert law. E) Comparison between experiment (solid lines) and expected decay (broken lines) from the Beer-Lambert law at 765 and 800 nm. The experimental data is not in agreement with simple linear absorption. This suggests additional processes, such as photon recycling, to occur which allow to maintain substantial photon intensity at large distances.

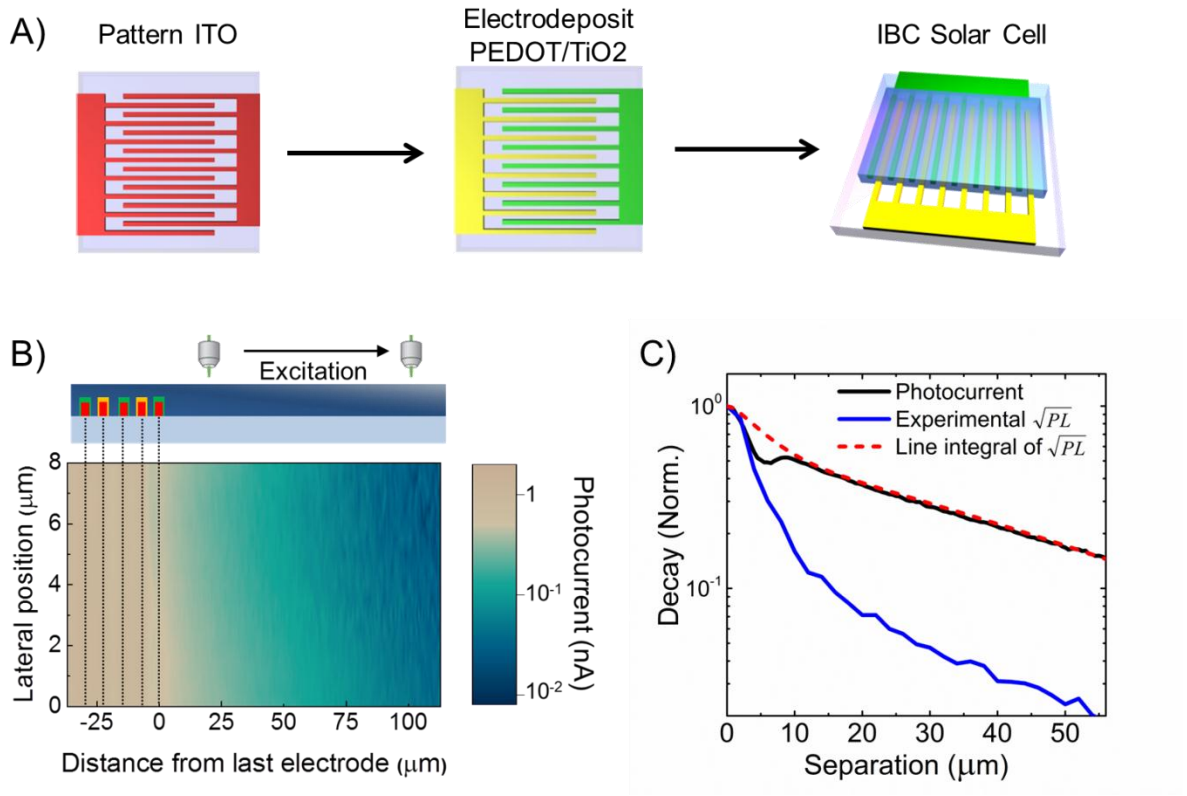

Fig. 2. Photocurrent mapping of an interdigitated back contact (IBC) perovskite solar cell. A) Fabrication process of IBC device: pattern a flat sheet of ITO, electrodeposit TiO2 on half the fingers and PEDOT on the other half, spincoat the photoactive perovskite layer. B) Photocurrent map at the edge of the active area of an IBC perovskite device. Lateral position along the electrode direction. We observe photocurrent several tens of microns beyond the last electrode (x-axis position 0 μm) C) Comparison between spatial decay of photocurrent and square root of PL. These results suggest that photon densities, which propagate over large distances through the material assisted by photon recycling, can be extracted as photocurrent.

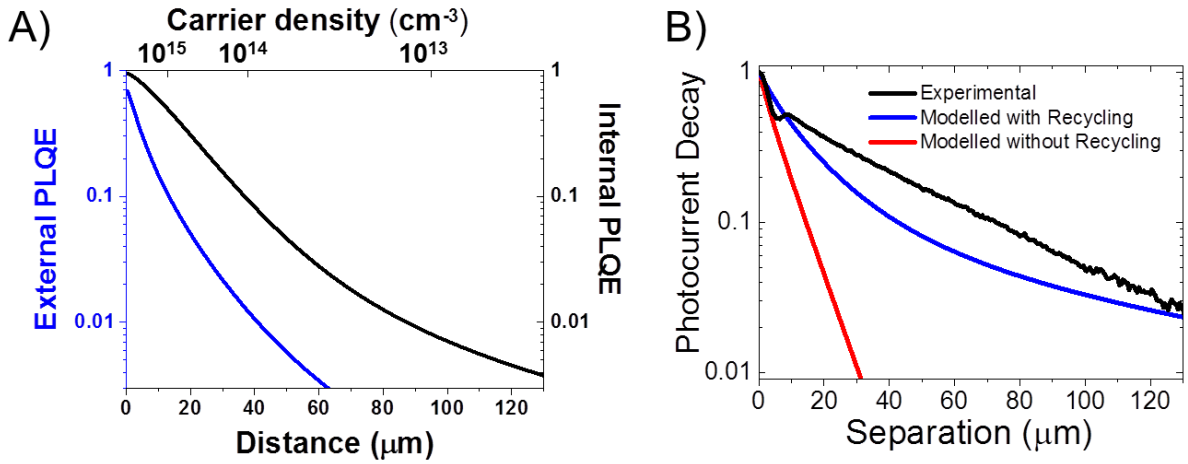

Fig. 3. A) Change in external and internal photoluminescence quantum efficiency (PLQE) as a function of distance derived from a photon recycling diffusion model as presented in the text, with reported mono- and bimolecular recombination (k_{mono} = 10^{6} s^{-1}, k_{bi} = 10^{-10} $cm^{3}s^{-1}$) and diffusion constants (D = 0.5 $cm^{2}s^{-1}$) of photoexcited carriers. B) Predicted spatial photocurrent decay for the model with and without photon recycling. We find that photon recycling is required to obtain the experimentally observed long extraction lengths.

Supplementary information:

Authors: Luis M. Pazos-Outón[1], Monika Szumilo[1], Robin Lambol[1], Johannes Richter[1], Micaela Crespo-Quesada[2], Mojtaba Abdi-Jalebi[1], Harry J. Beeson[1], Milan Vrucinic[1], Mejd Alsari[1], Henry J. Snaith[4], Bruno Ehrler[3], Richard H. Friend[1,*] and Felix Deschler[1,*].

Affiliations:

[1]Cavendish Laboratory, University of Cambridge, JJ Thomson Avenue, CB3 0HE, Cambridge, UK

[2]Department of Chemistry, University of Cambridge, CB2 1EW, Cambridge, UK.

[3]FOM Institute AMOLF, Center for Nanophotonics, Science Park 104, 1098 XG Amsterdam, The Netherlands.

[4]Clarendon Laboratory, Department of Physics, University of Oxford, OX1 3PU, Oxford, UK.

*Correspondence to: rhf10@cam.ac.uk and fd297@cam.ac.uk

Supplementary Materials:

Materials and Methods

Supplementary text

Figures S1-S19

References (1-15)

Materials and Methods:

Perovskite deposition and thickness measurement

All materials were purchased from Sigma-Aldrich or Acros Organics and were used as received. A solution of Pb(Ac)2 and CH3NH3I having molar ratio of 1:3 were prepared in N,N-dimethylformamide solvent by constant stirring for 5 min. The solution was then spincoated on top of clean Spectrosil glass substrate (for confocal PL measurements) or on top of the interdigitated selective electrodes (for combined PL and photocurrent measurements) at 2000 rpm for 60 seconds (accel. of 2000 rpm s-1) and annealed at 100 °C for 5 min to achieve laterally uniform perovskite films. The thickness of the films was measured with a Veeco Dektak profilometer.

Interdigitated back contact device fabrication

Samples for photocurrent measurement were prepared on pre-fabricated selective bottom contact substrates. Glass substrates covered with a flat film of ITO were cleaned by sonication in acetone (10 minutes) and IPA (7 minutes) and dried with a nitrogen blow gun. A layer of S1813 photoresist was deposited, exposed and developed in MF 319 developer leaving a pattern of interdigitated electrodes (see, Figure 2A). The width of each electrode was 4μm with 4μm spacing. The total active area covered with the interdigitated electrodes measured 1.5 x 0.8 mm. (188 fingers of 0.8 mm length. Following the developing step, the sample was etched in 32%

HCl for 11 minutes on a rotating holder to facilitate a constant flow of etchant. Resist was removed by soaking in acetone. The sample was then rinsed with IPA and dried with a nitrogen blow gun.

Electron and hole selective layers of TiO2 and PEDOT were deposited on the electrodes by electrodeposition. The electrodeposition of TiO2 was performed following the experimental procedure reported in (*1*). Briefly, an aqueous solution containing 0.02 M of TiOSO4 (Sigma), 0.03 M H2O2, and 0.1 M KNO3 (Sigma) was cooled and kept at 10 °C while N2 was flown through the solution. A standard three-electrode configuration was used, with ITO conductive glass as working electrode, Pt mesh as counter electrode and an Ag/AgCl reference electrode. The cathodic electrodeposition was carried out between -1.15 V and -0.95 V vs. Ag/AgCl for times ranging from 200 s to 1400 s, which led to the formation of TiO(OH)2 · xH2O gel film on the electrode. Subsequently, this film was subjected to heat treatment in air at 400 °C for 1 h (heating rate 10 °C min-1) to obtain polycrystalline TiO2 thin films.

Electropolymerisation of poly-3,4-ethylenedioxythiophene (PEDOT) on the remaining fingers was conducted using 0.01 M 3,4-ethylenedioxythiophene (EDOT) monomer (Sigma Aldrich) and 1.0 M LiClO4 (Acros) electrolyte in propylene carbonate (Sigma Aldrich), contained in a sealed chamber through which N2 was bubbled prior to deposition. A three-electrode configuration was used, with ITO conductive glass as the working electrode, Pt foil as the counter electrode and an Ag pseudo-reference electrode. An Fc/Fc+ redox couple measured in the same conditions as used for electropolymerisation displayed an equilibrium potential of +0.16 V. The anodic polymerisation was carried out at approximately +1.2 V vs. Ag for 1 s. After deposition, the film was rinsed with acetonitrile and dried with N2.

PL and photocurrent measurements

Combined photoluminescence and photocurrent was measured using a WITec alpha 300 s setup. The excitation source was 405 nm cw laser (Coherent CUBE), chopped using a Stanford Research SR 540 chopping unit at frequency of 840Hz. The light was coupled though an optical fibre to the microscope and focused using 60x Nikon lens (NA = 0.7). Sample rested on a X-Y piezo stage of the microscope. The PL signal was collected in reflection mode with the same 60x objective and detected using a spectrometer fitted with a CCD detector. A low pass filter with a cut-off wavelength of 435 nm was fitted before the CCD detector to block the excitation component of transmitted light (405nm). For the photocurrent detection micro needle probes were used to feed the signal from sample electrodes into a Stanford Research SR 570 preamplifier. The signal from the preamplifier was detected with a Stanford Research SR 830 lock-in amplifier (locked-in with the chopper) as current intensity and phase shift. By movement of the sample stage, maps of combined PL and photocurrent were recorded at the edges of the pixels (last electrodes) with scan direction both parallel and perpendicular to the electrodes.

In a confocal configuration used for measurements of PL decay with distance light transmitted through the sample was collected with a 40x objective (NA = 0.6). The collecting lens can be moved in x, y and z directions which allows to maximise the collected PL intensity. By the translational movement of the collecting lens from this point of maximum intensity it is possible to separate excitation and collection spot with 0.1 µm stage accuracy, keeping the excitation spot in place. By simultaneous movement of the sample stage and collecting lens (in opposite

directions) it is possible to change the separation of the excitation and collection spots, keeping collection spot stationary and moving excitation spot away. Individual spectra were recorded.

All movements of the stage and lenses are controlled from the WITec ScanCtr Spectroscopy Plus software in which also all spectral and photocurrent data is recorded. All measurements were performed in N2 atmosphere. All PL spectra were measured over 10 averages.

PDS and UV-Vis

For PDS measurements, a monochromatic pump light beam is shone on the sample (film on Quartz substrate), which on absorption produces a thermal gradient near the sample surface via non-radiative relaxation induced heating. This results in a refractive index gradient in the area surrounding the sample surface. This refractive index gradient is further enhanced by immersing the sample in an inert liquid FC-72 Fluorinert® (3M Company) which has a high refractive index change per unit change in temperature. A fixed wavelength CW laser Probe beam is passed through this refractive index gradient producing a deflection proportional to the absorbed light at that particular wavelength, which is detected by a photo-diode and lock-in amplifier combination. Scanning through different wavelengths gives the absorption spectra. We note that this technique is not affected by scattering and interference effects, but is only sensitive to non-radiative relaxation processes in the sample.

Photoluminescence excitation measurements

Photoluminescence excitation measurements were performed by exciting the sample under inert conditions with monochromatic light which was generate by passing the broad band emission from a halogen lamp through a monochromator. The emission was spectrally resolved by passing it through a monochromator and detection on a CCD camera. A narrow emission range was selected to quantify the emission intensity, while the excitation was scanned by varying the excitation monochromator grating position. The PLE spectrum was corrected for variations in the excitation intensity by detecting the intensity of the excitation with a reference photodiode.

Time-resolved photoluminescence

Time-resolved photoluminescence measurements were taken with a gated intensified CCD camera system (Andor iStar DH740 CCI-010) connected to a grating spectrometer (Andor SR303i). Excitation was performed with femtosecond laser pulses which were generated in a homebuilt setup by second harmonic generation (SHG) in a BBO crystal from the fundamental output (pulse energy 1.55 eV, pulse length 80 fs) of a Ti:Sapphire laser system (Spectra Physics Solstice). The laser pulses had an energy of 3.1 eV and a fluence of 5 nJ/cm2. Temporal resolution of the PL emission was obtained by measuring the PL from the sample by stepping the iCCD gate delay for different delays with respect to the excitation. The gate width was 20 ns.

IV measurements

Current-voltage (IV) characteristics were measured in the dark and under a solar simulator (Oriel 92250A) using a Keithley 2636A source-measure unit. The current from the solar cell was compared to the current of a NIST-traceable calibrated photodiode (Thorlabs SM05-CAL). Both the device and the calibration cell were measured against a reference diode (Thorlabs SM05) to account for changes in light intensity between the measurements.

Supplementary text:

A. Cyclic voltammetry of electrodeposited selective electrodes

Figure S2 shows a representative cyclic voltammogram (CV) for the electropolymerisation of PEDOT on ITO. The CV shows a strong rise in current around +1.2V as polymerisation starts on the forward scan, with a current crossover on the reverse scan indicative of nucleated growth. There is then a peak in current around -0.8V on the reverse scan, which probably corresponds to de-doping of the PEDOT film, with the re-doping giving current peaks around -0.4V on the forward scan. These redox features are similar to those found in the literature (*2*). Since the polymerisation was conducted in the non-aqueous solvent propylene carbonate, an Ag wire pseudo-reference electrode was used. In order to calibrate this, 0.01M ferrocene was added to the electropolymerisation solution and the Fc/Fc+ redox couple was measured. The cyclic voltammogram shown in the figure gives the Fc/Fc+ equilibrium potential to be +0.16V.

Figure S3 shows a representative cyclic voltammogram (CV) for the electrodeposition of TiO2 on ITO. It can be observed that a current crossover occurs on the first two backward scans. After this potential, the current of the backward scan becomes more negative than the forward scan, which is consistent with the thermodynamics of nucleation and growth phenomenon (*3*). Indeed, the deposition of new Ti(IV) species probably requires less energy on existing nuclei than the creation of new ones (1). The subsequent scans, as well as those performed after the electrodeposition show a characteristic cathodic wave at a potential of approximately -0.85 VAgAgCl, consistent with the reduction of nitrate moiety (*4*). The steps involved in the electrosynthesis of TiO2 can be described as follows: TiOSO4 is solubilised due to the presence of H2O2. For the hydrolysis of the precursor, Ti(O2)SO4, OH- ions are consumed, which are in turn generated at the substrate/electrolyte interface by the reduction of nitrate when potentials more negative than -0.85 VAgAgCl are applied (*4*) The film that is created on the substrate is partially dehydrated polymeric titanium Ti(IV) hydroxide (*5*).This material is then transformed into TiO2 by firing.

B. XPS analysis of selective electrodes

XPS analysis was performed on the electrodeposited PEDOT and TiO2 layers (Figure S4 and S5). XPS data for PEDOT is shown in Figure S4. The S 2p region of the XPS spectrum exhibits a doublet at 162.4 eV and 163.5 eV, corresponding to the S 2p3/2 and 2p1/2 features respectively (*6*). There is a third feature centered around 165.2 eV, 1.7 eV higher than the main peak at 163.5 eV. This closely matches the π-π* transition bandgap (*7*), and hence is likely a 'shake-up' feature (*6*).

The O 1s region of the spectrum exhibits three features, namely the main C-O-C peak at 531.9 eV (*8*), a small peak at 534.3 eV, and a third peak at lower binding energies, which can be attributed to the ClO4- counter-ion (*8*). Indeed, the magnitude of this third peak signal relative to

the first decreases for films which have been partially or fully de-doped by applying a negative potential after electropolymerisation (not shown here).

The C 1s region of the spectrum shows a main peak at 285.1 eV, which is likely to arise from the C-O-C and C=C-O bonds, a second peak at 283.6 eV, which corresponds to C-C and C-S bonds, and a 'shake-up' feature at 286.8 eV (*5*).

XPS data for TiO2 is shown in Figure S5. Static charge developed on the sample. To overcome this problem, all binding energies were referenced to the C1s peak at 284.6 eV of the surface adventitious carbon.

The Ti 2p region is characterised by a doublet at 458.1 and 463.8 eV, corresponding to Ti 2p3/2 and Ti 2p1/2, and satellites at 472 and 477 eV. The Ti 2p3/2 binding energy exceeds that of Ti metal (454.0 eV), TiO (455.0 eV), and Ti2O3 (456.7 eV) (*9*). On the other hand, Ti 2p3/2 in TiO2 has been reported to be 458.0-458.7 eV (*9-12*), suggesting that Ti is in the Ti4+ oxidation state and directly bonded to oxygen. Furthermore, the doublet separation between the 2p3/2 peak and Ti 2p1/2 peak is in good agreement with the reported value of 5.7 eV for anatase phase TiO2 thin films deposited by MOCVD (*13*).

The region for O 1s was resolved into two components, namely the main peak at 529.7 eV, corresponding to TiO2 and the peak at 531.3 eV, which can be attributed to Ti-OH species (*11, 14*). While the latter is predominant in as-deposited TiO2 amorphous thin films, it is also present in commercially available crystalline TiO2 (*11*). This suggests that the titanium hydroxide gel layer formed during electrodeposition was successfully transformed into TiO2 upon annealing.

Quantitative XPS analysis determined an atomic ratio of Ti:O of 2.35, which is slightly higher than the value found by Gao et al of 1:2.162, but lower than that of amorphous TiO2 layer deposited from an aqueous peroxotitanate (1:2.6) (*9*). The difference can be potentially ascribed to surface contamination by oxygenated species.

The fact that the XPS analysis proves the presence of TiO2 and that its transformation to crystalline anatase phase has been reported to start at temperatures from 300 °C4 to 400 °C (*9*), indicates that the electrodeposited TiO2 layers were crystalline. It was, however, not possible to detect the anatase phase by XRD analysis due to the low thickness of the layers.

C. Optical images and AFM scans of selective electrodes

Figures S6 and S7 show optical microscopy and atomic force microscopy images of the electrodeposited PEDOT and TiO2 layers. Both layers can be seen clearly under the optical microscope and were found to cover the contacted ITO uniformly. AFM scanning showed an average thickness of 35 nm for PEDOT and 15 nm for TiO2.

D. Discussion of JV curves

Figure S14 presents JV characteristics for the IBC device. At a reverse bias the photocurrent increases strongly, likely due to an enhanced selectivity at the electrodes interface. To illustrate the effect of our selective electrodes, we pre-biased the device in forward bias at 2V for 30 seconds before doing the sweep, and observed an enhanced photocurrent generation at short-circuit with a stronger diode-like behavior. Several reports suggest that this enhancement comes from a re-distribution of ions in the film, which forms a p-i-n junction. The presence of those ions at the interface can form a local electric field which enhances generation. Indeed, in our pre-biased measurement we observe a slight decrease of the photocurrent when going into reverse bias, probably due to ion relaxation which breaks the electric field. For comparison, characterization of a lateral solar cell without selective layers is shown in Figure S15, which shows a significant reduction in charge selectivity and reduced voltage and photocurrent.

E. Details of emission and photocurrent model

The coupled differential equations of the model have to describe the following processes: charges (n) are generated by all incident photons (G) at the excitation spot, diffuse, are regenerated by absorption of photons in the perovskite (γ_λ), and recombine with mono/bimolecular rates k_1, k_2. Photons in the perovskite γ_λ are generated by bimolecular recombination of charges, propagate and get absorbed. This gives the coupled differential equations:

$$\frac{dn}{dt} = \mathrm{G} + D\nabla^2 n + \frac{c}{n_s}\sum_\lambda \alpha_\lambda \gamma_\lambda - k_1 n - k_2 n^2$$

$$\frac{d\gamma_\lambda}{dt} = (k_2 n^2 P_{stay})P_\lambda + D_\lambda \nabla^2 \gamma_\lambda - \frac{c}{n_s}\alpha_\lambda \gamma_\lambda$$

where D represents the relevant diffusion/propagation coefficients, n_s the refractive index of lead iodide perovskite, c the speed of light, α_λ the measured wavelength-dependent absorption constant of the material, k_1 the 1st order (monomolecular) recombination constant, k_2 the 2nd order (bimolecular) recombination constant, P_{stay} the probability that photons will be emitted at angles that lead to total internal reflection (guiding of photons in the film). P_λ the probability that light will be emitted at wavelength λ, which is determined from normalized steady state PL spectra. It is assumed that the wavelengths will be quantised for numerical solution purposes. The excitation profile of the laser G is taken as a Gaussian distribution of full-width half maximum 1.5 µm. $D_\lambda = \frac{c}{n_s}\frac{1}{3\alpha}$ for photon transport. These parameters are taken from spectroscopic data and published results, or can be easily calculated:

Photons will either leave at the air interface or be absorbed at the perovskite interface – we ignore them in the first case and only consider the second sort. We will ignore the moderate wavelength-dependence of refractive indices and use a value of 2.5 for the perovskite, 1 for air and 1.5 for the glass. We can calculate the proportion of photons leaving the perovskite layer using the angle-dependent transmission coefficients for parallel and perpendicular light polarisations.

$$T_{\parallel} = 1 - \left(\frac{n_2 \cos\theta - n_1 \cos\theta_t}{n_2 \cos\theta + n_1 \cos\theta_t}\right)^2$$
$$T_{\perp} = 1 - \left(\frac{n_1 \cos\theta - n_2 \cos\theta_t}{n_1 \cos\theta + n_2 \cos\theta_t}\right)^2$$

for θ_t the angle of emission after transmission, n_1 the internal and n_2 the external refractive indices. This goes to 0 for angles over the critical angle. We multiply this by the wavelength-dependent probability that the photon has not been absorbed before travelling the required distance to make it to an interface. The photons are then reflected towards the other interface, with further absorption and chance of transmission there and so on. Integrating over all emission angles, possible starting positions and for the spectral range of the PL, we find that the optical probability of escape (1-P_{stay}) is 12.5%.

F. Comparison modeled charge density results with photocurrent experiments

The diffusive current from the excitation spot detected at the electrodes may be approximated as the integral $I(x) \propto \int_x^{\infty} n(r)dl$ for dl being a differential element of the 2nd electrode, which limits the charge. We can approximate this as:

$$I(x) \propto \sum_{r_i \geq x} n(r_i)\left(\sqrt{r_{i+1}^2 - x^2} - \sqrt{r_i^2 - x^2}\right).$$

G. Calculation of internal photon density under photon recycling:

The internal intensity can be estimated using the geometrical series:

$$Internal\ Intensity\ = I_{sun} \sum_{r=0}^{\infty} (Confinement\ Factor \cdot PLQE)^r$$

Solving the series:

$$Internal\ Intensity\ = \frac{I_{sun}}{1 - Confinement\ Factor \cdot PLQE}$$

The evaluation of this formula for the standard charge carrier density in a perovskite device (~10^{15} cm^{-3}), a PLQE of ~60%, according to our model in Figure 3A, and a confinement factor of (1-1/4n^2), gives an internal intensity of ~2.

The internal excitation density in a perovskite film can go well beyond 1 sun, potentially reaching 23 suns assuming 100% PLQE and a confinement factor of (1-1/4n^2). In GaAs this

number is 48, mostly because of a higher refractive index which leads to a higher confinement factor.

References

(1) Karuppuchamy, S. et al. Cathodic electrodeposition of TiO2 thin films for dye synthesized photoelectrochemical applications Chem. Lett., 1, 78 (2001)

(2) Kvarnström, C.et al., In situ spectroelectrochemical characterization of poly(3,4-ethylenedioxythiophene) Electr. Act., 44(16), 2739 (1999)

(3) Hezard, T. et al. Gold nanoparticles electrodeposited on glassy carbon using cyclic voltammetry: Application to Hg(II) trace analysis. J. Electroanal. Chem. 664, 46–52 (2012).

(4) Silva, N. et al. Electrosynthesized TiO2 films: dependence of the brookite–anatase ratio on the applied potential. J. Mater. Sci. 49, 2952–2959 (2014).

(5) Kavan, L., Oregan, B., Kay, A. & Gratzel, M. Preparation of Tio2 (Anatase) Films on Electrodes by Anodic Oxidative Hydrolysis of Ticl3. J. Electroanal. Chem. 346, 291–307 (1993).

(6) Moulder, J.F.; Stickle, W.R.; Sobol, P.E.;K.D. Bomben, K.D. Handbook of X-ray photoelectron spectroscopy: A reference book of standard spectra for identification and interpretation of XPS data. Physical Electronics: Eden Prairie, MN, 1992.

(7) Groenendaal, L.; Jonas, F.; Freitag, D.; Pielartzik, H.; Reynolds, J.R. Poly(3,4-ethylenedioxythiophene) and Its Derivatives: Past, Present and Future, Advanced Materials, 2000, 12, 7, 481.

(8) Spanninga, S.A.; Martin, D.C.; Chen, Z. X-ray Photoelectron Spectroscopy Study of Counterion Incorporation in Poly(3,4-ethylenedioxythiophene), Journal of Physical Chemistry C, 2009, 113, 5585.

(9) Gao, Y., Masuda, Y., Peng, Z., Yonezawa, T. & Koumoto, K. Room temperature deposition of a TiO2 thin film from aqueous peroxotitanate solution. J. Mater. Chem. 13, 608–613 (2003).

(10) Yu, J. C., Yu, J. G., Ho, W. K., Jiang, Z. T. & Zhang, L. Z. Effects of F- doping on the photocatalytic activity and microstructures of nanocrystalline TiO2 powders. Chem. Mater. 14, 3808–3816 (2002).

(11) Tomaszek, R. et al. Microstructural characterization of plasma sprayed TiO2 functional coating with gradient of crystal grain size. Surf. Coat. Technol. 201, 45–56 (2006).

(12) Saini, K. K. et al. Structural and optical properties of TiO2 thin films derived by sol–gel dip coating process. J. Non. Cryst. Solids 353, 2469–2473 (2007).

(13) Babelon, P. et al. SEM and XPS studies of titanium dioxide thin films grown by MOCVD. Thin Solid Films 322, 63–67 (1998).

(14) Binetti, E., El Koura, Z., Patel, N., Dashora, A. & Miotello, A. Rapid hydrogenation of amorphous TiO2 to produce efficient H-doped anatase for photocatalytic water splitting. Appl. Catal. A Gen. 500, 69–73 (2015).

(15) Saba, M. et al. Correlated electron-hole plasma in organometal perovskites. Nat. Comm. 5, 5049 (2014)

Figures

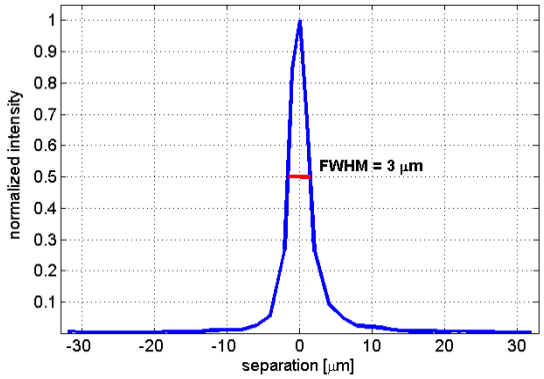

Fig. S1 Intensity map of detected laser light around the excitation spot in a film. Each data point was obtained by integration of detected light at the laser wavelength as detected with a bottom lens at different separation from the exciting top lens. The measurement shows that the spatial resolution of our measurement is ~1.5um.

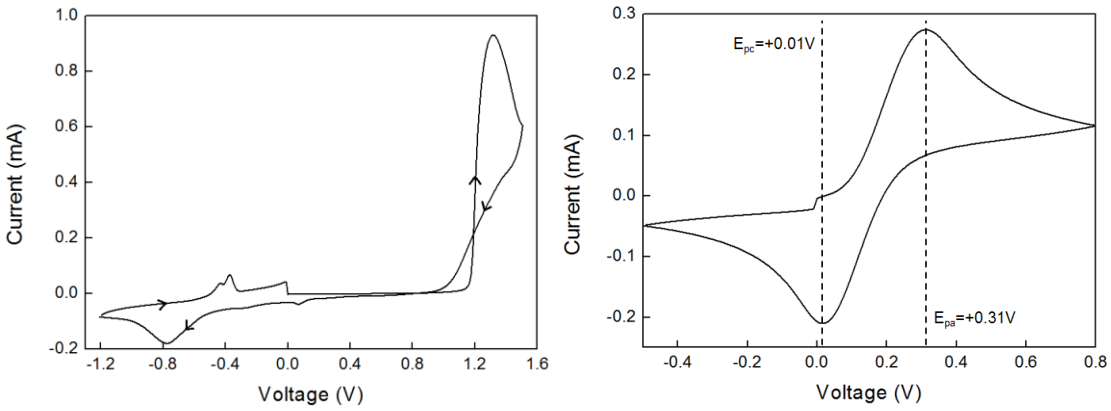

Fig. S2 Left: Initial voltagrammogram for the electropolymerisation of PEDOT recorded at an ITO electrode in a 0.01M EDOT, 1.0M LiClO4 propylene carbonate solution at a scan rate of 50mV/s. Right: Cyclic voltammogram showing the Fc/Fc+ redox reaction in a 0.01M ferrocene, 0.01M EDOT, 1.0M LiClO4 propylene carbonate solution at a scan rate of 50mV/s.

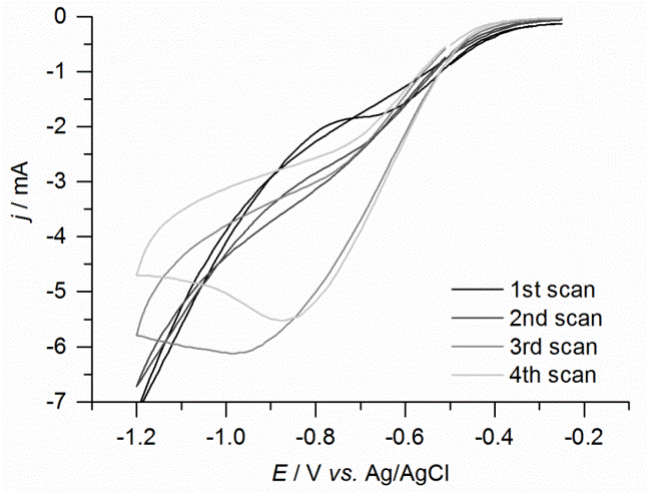

Fig. S3 Cyclic voltammogram (CV) for the electrodeposition of TiO2 on ITO. Initial CV for the electrodeposition of TiO2 recorded at an ITO electrode in a 0.02 M of TiOSO4, 0.03 M H2O2 and 0.1 M KNO3 solution at 10 °C and a scan rate of 100 mV s-1.

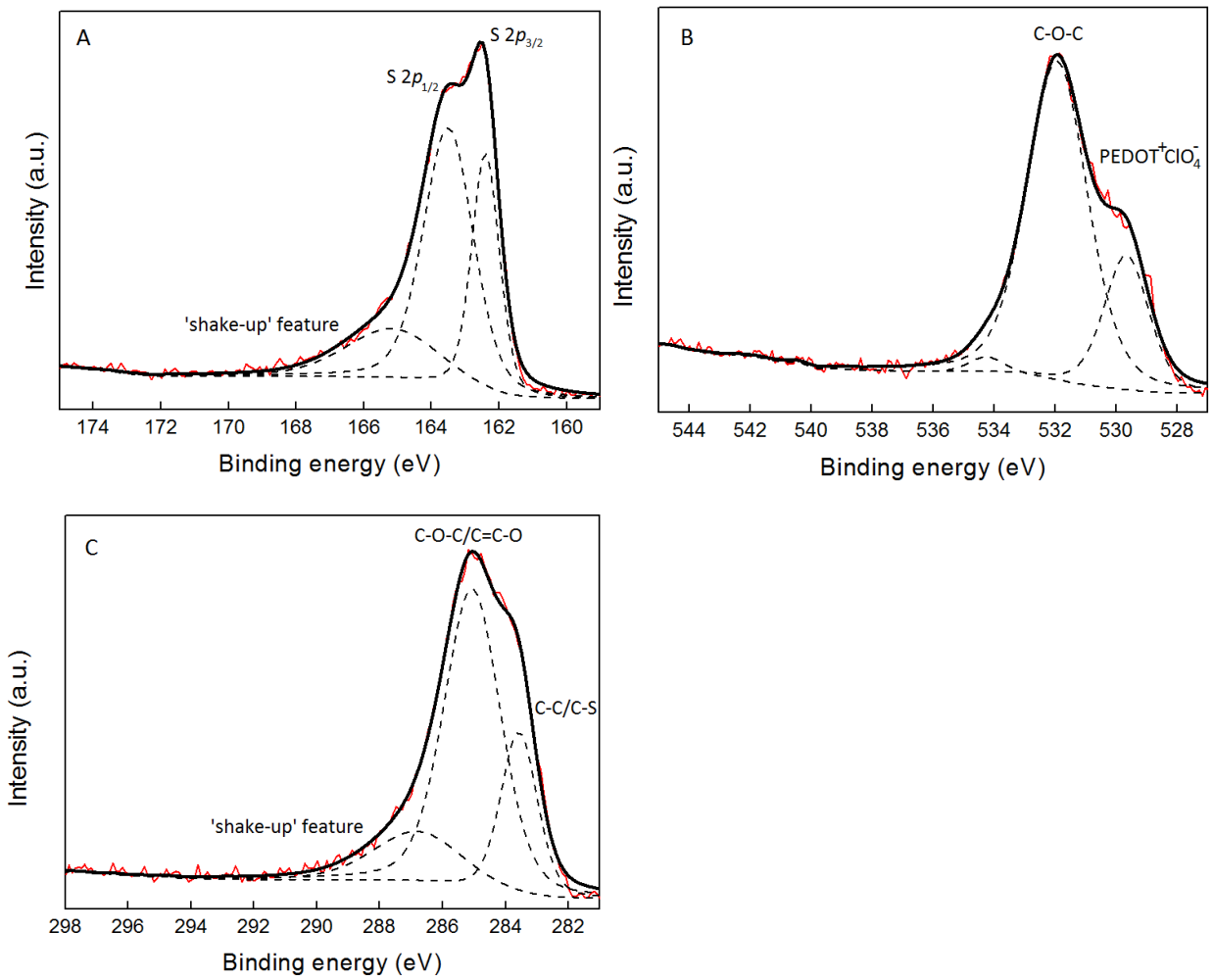

Fig. S4 XPS characterization of electropolymerized PEDOT. A) S 2p, B) O 1s and C) C1s high resolution XPS spectra of the electropolymerized PEDOT on ITO. The film was left in its as-prepared, 'doped' state.

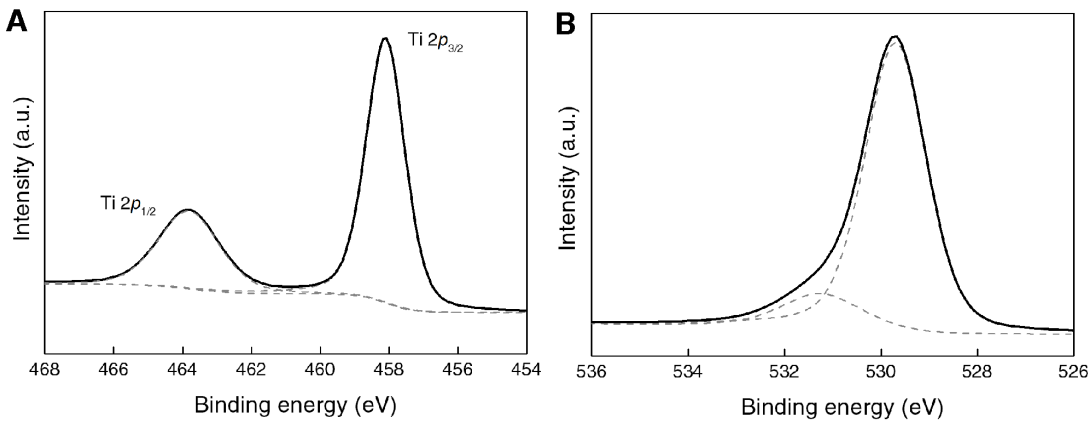

Fig. S5 XPS characterization of the TiO2 film. A) Ti 2p and B) O 1s high resolution XPS spectra of the electrodeposited TiO2 layer on ITO after annealing at 400 °C for 1h.

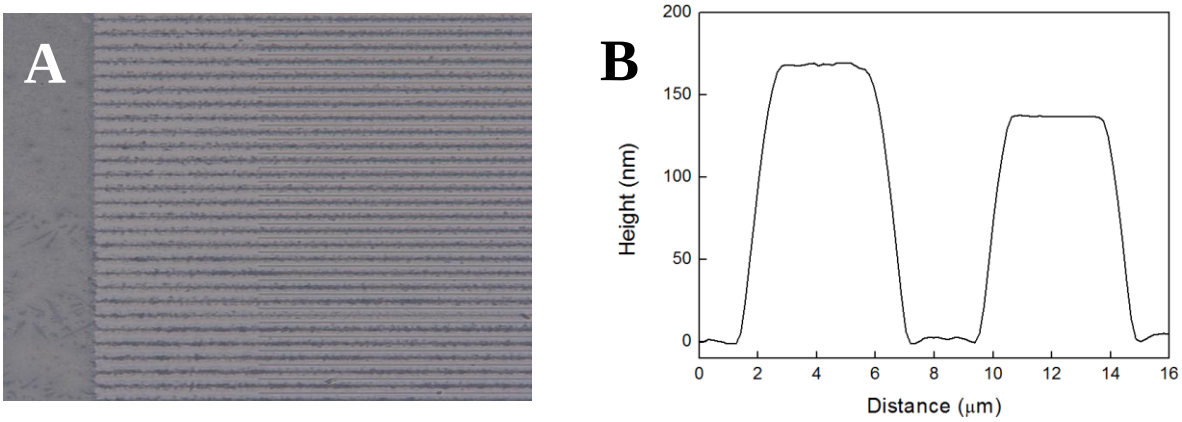

Fig. S6 Characterization of the PEDOT film. A, Optical image (x20) of selectively deposited PEDOT. This PEDOT is made particularly thick on purpose, in order to be visible in the optical microscope. B, AFM Image of PEDOT vs Flat ITO. The PEDOT thickness is around 35 nm for a deposition at 1.25 V for 1s.

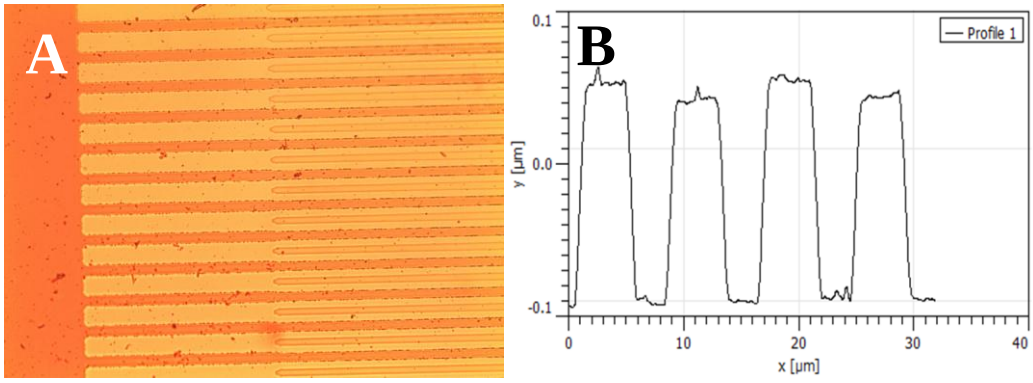

Fig. S7 Characterization of the TiO2 film. A) Optical image (x50) of selectively deposited TiO2 (dark fingers). The fingers on the right are bare ITO. B) AFM Image of selectively deposited TiO2 with an average thickness of 15 nm. Conditions: 0.02 M of TiOSO4, 0.03 M H2O2 and 0.1 M KNO3, 10 °C, -0.95 VAgAgCl, 400 s.

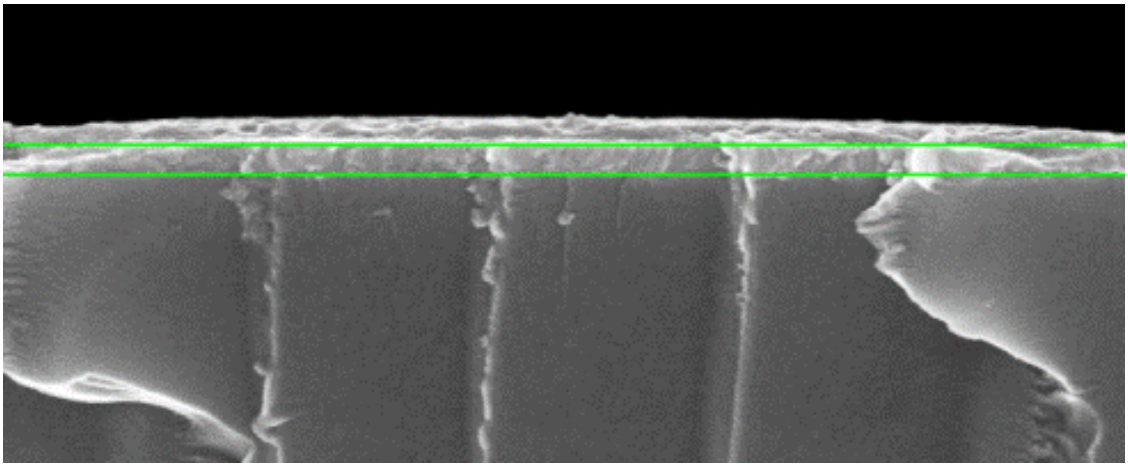

Fig. S8 SEM cross-section of perovskite layer deposited on top of an ITO electrode. The horizontal bars show the thickness of the ITO layer – 125 nm. A good conformity of perovskite layer to the shape of the electrodes can be observed.

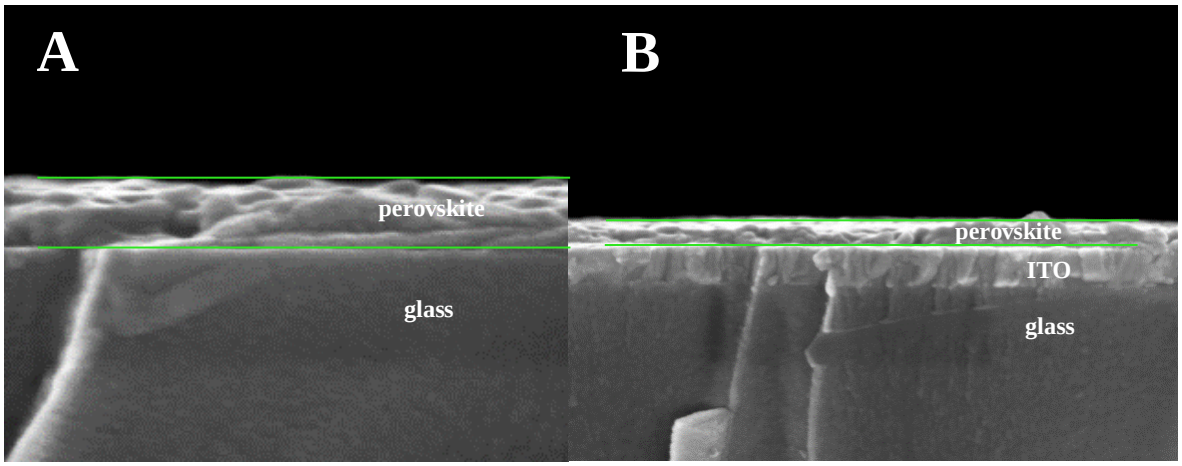

Fig. S9 SEM cross-sections of perovskite layer on glass (A) and ITO (B). The horizontal bars show the thickness of the layer – ~109 nm. Perovskite forms a continuous film on both substrates.

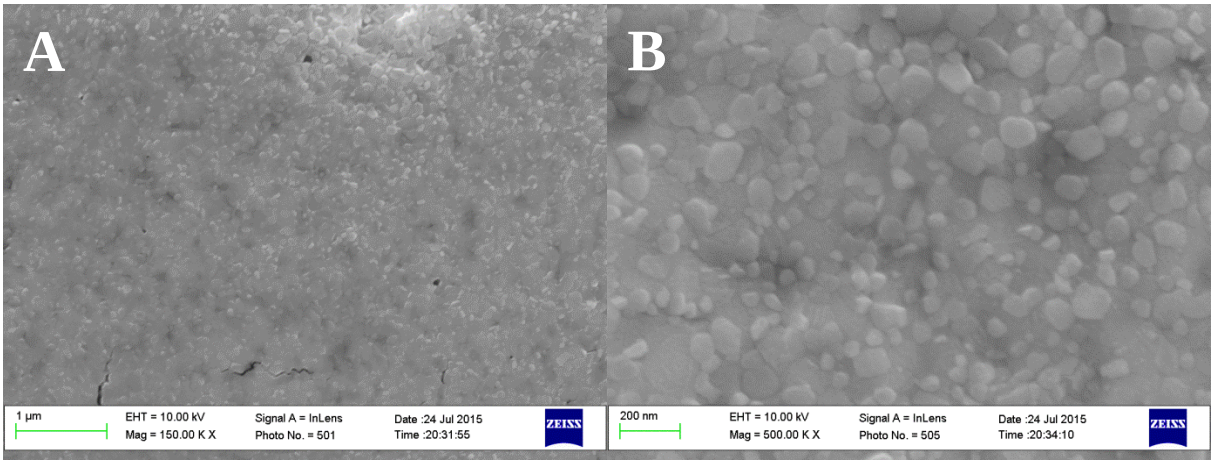

Fig. S10 SEM - top view of perovskite layer on top of the PEDOT electrode. The scale bar is 1µm (A) and 200 nm (B).

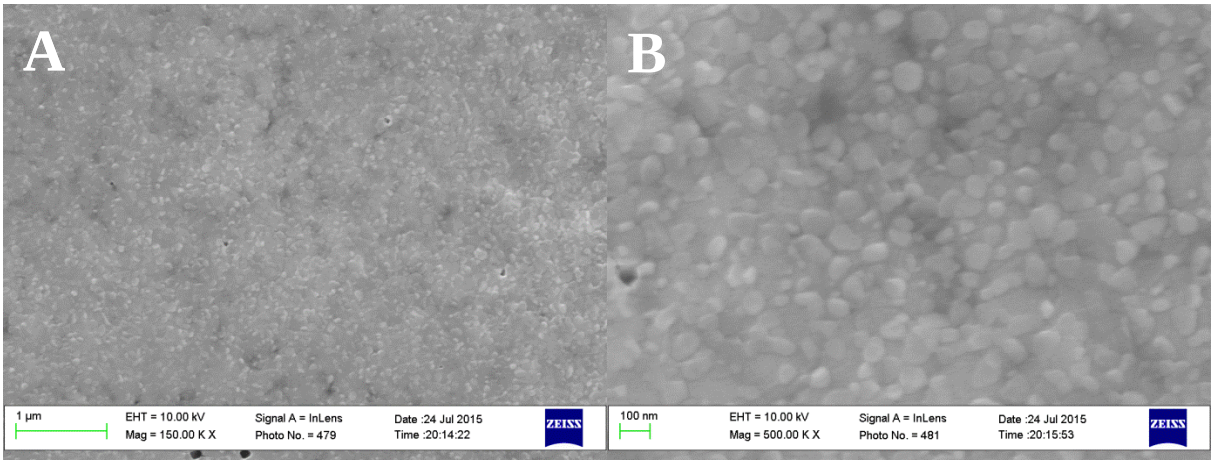

Fig. S11 SEM - top view of perovskite layer on TiO2 electrode. The scale bar is 1 µm (A) and 100nm (B).

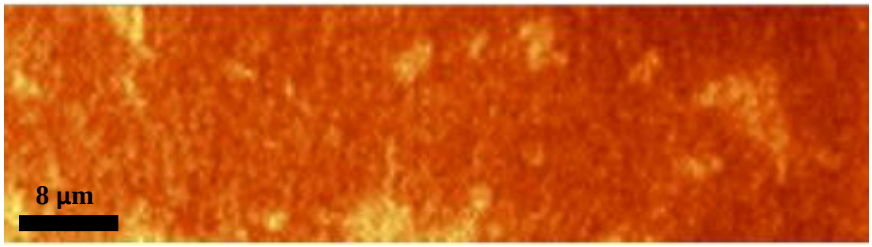

Fig. S12 Light transmission map of a typical perovskite film.

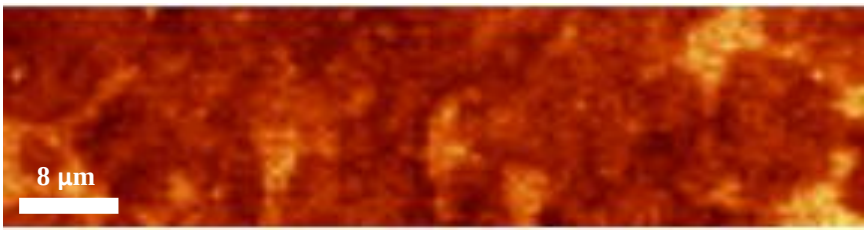

Fig. S13 PL map of a typical perovskite film.

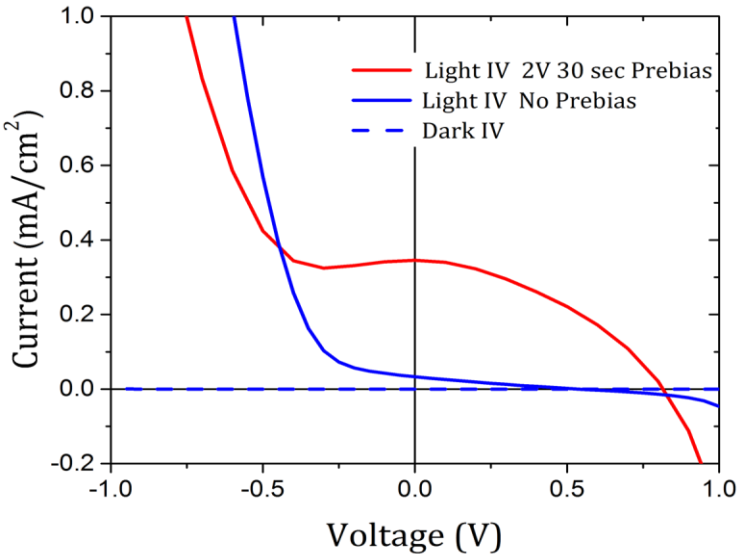

Fig. S14 JV characteristics for IBC device with and without prebiasing

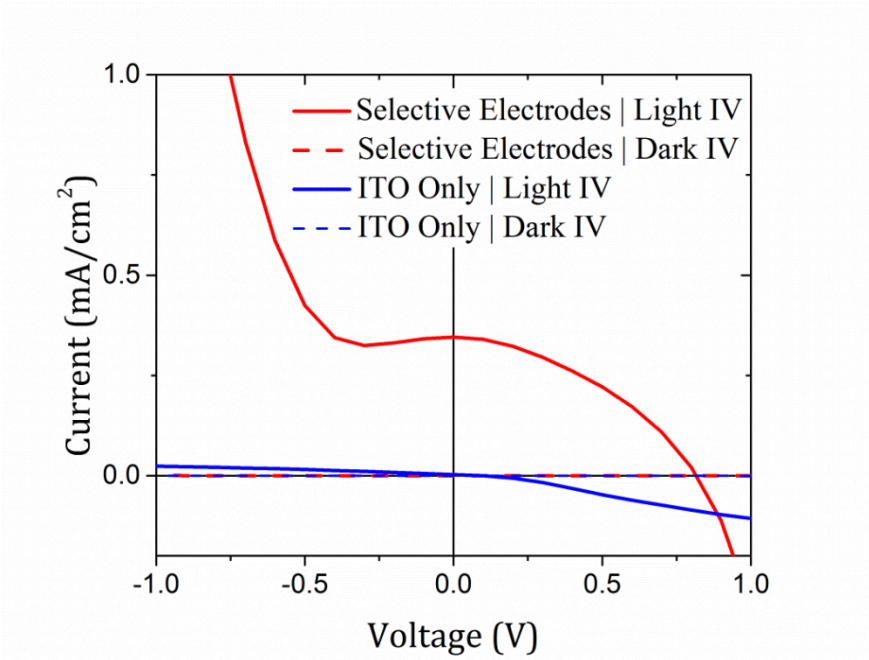

Fig. S15 Comparison of the JV characteristics between IBC devices with and without selective electrodes. Upon addition of selective electrodes significant increase in charge selectivity and increased voltage and photocurrent can be observed.

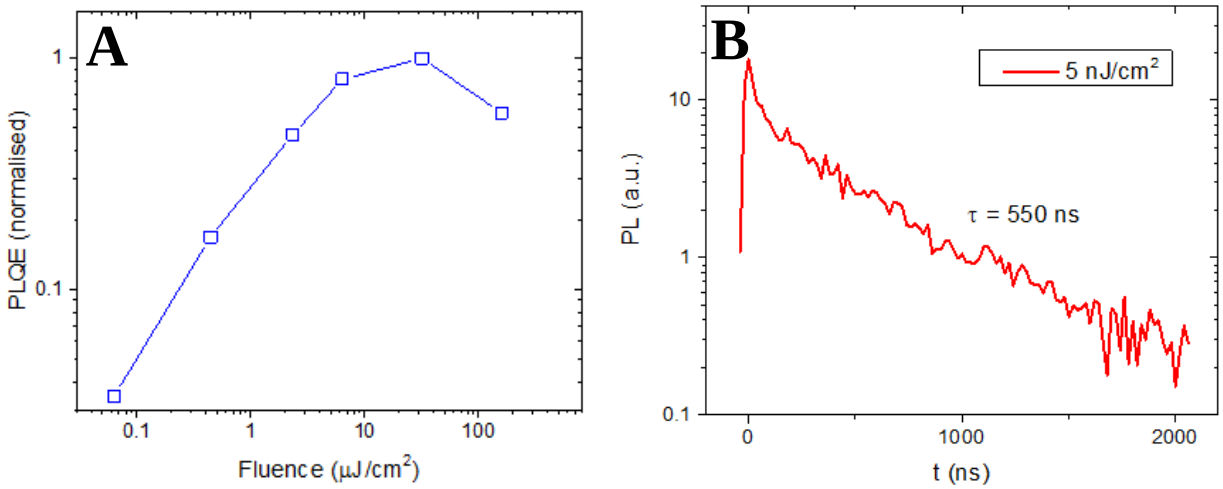

Fig. S16 A. Fluence dependence of external photoluminescence quantum efficiency after pulsed excitation. The PLQE strongly depends on the excitation fluence due to the competition of radiative and non-radiative decay channels (*15*). B. Transient photoluminescence of 100 nm film measured with an ICCD after excitation with a 100 fs 400nm laser pulse. The sample shows a PL lifetime of 550 ns which corresponds to a carrier lifetime of 1.1 μs assuming that the PL originates from a bimolecular recombination process

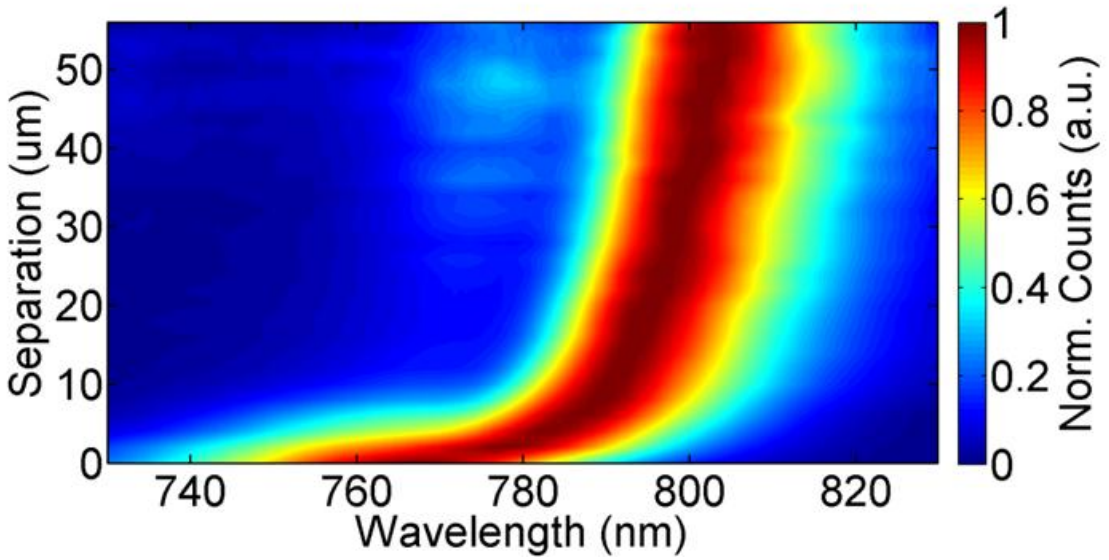

Fig. S 17 Normalized photoluminescence change with increasing separation of excitation and collection lenses in perovskite film. The red component of the spectrum, dominating at separation larger than ~5 μm, is accompanied by a weaker peak close to the original emission at 765 nm. This bluer feature can be a signature of recycled (and guided) photons.

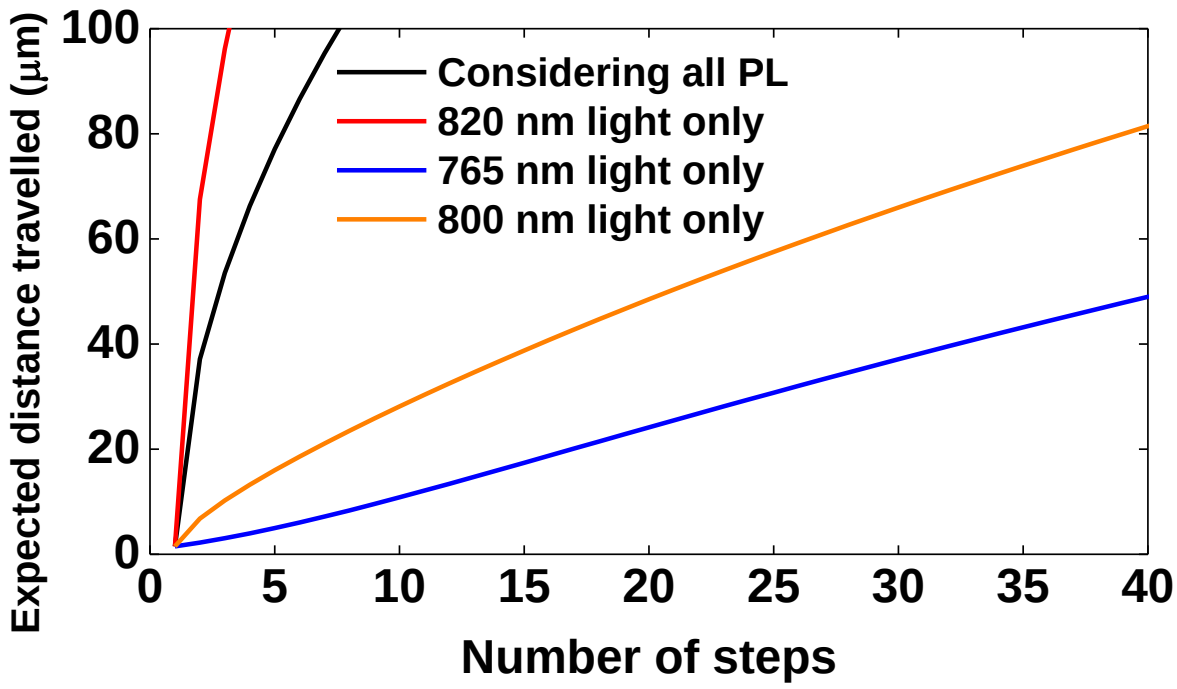

Fig. S18 Modelled charge carrier travel distance for a given number of recycling steps as estimated from a simple step-count model.

This simulation is designed to give an intuitive single-particle perspective on the recycling. From the PL we can estimate carrier density, as bluer components of light must be locally generated. This gives us $n \propto LE(\lambda > \lambda_0)/PL(\lambda > \lambda_0)$ for LE the light emitted and λ_0 given by the experimental values over which *LE/PL* is roughly constant. We set the absolute value of n using a diffusionless balance between recombination and generation. We use this distribution to fit the decay time τ for the particles, $\frac{1}{\tau} = k_1 + k_2 n$. During this time the particles move $\langle \Delta x^2 \rangle = 4D\tau \sim 16^2 \mu\text{m}^2$ (for D = 0.5 cm^2/s) at large distances. As light, the particles move $\langle \Delta x_{light}^2 \rangle = \frac{2}{3}\int_0^\infty dx\, x^2 \alpha e^{-\alpha x} \int PL.d\lambda = \frac{2}{3}.2\int \frac{PL}{\alpha^2} d\lambda \approx (37\mu\text{m})^2$, where the 2/3 factor comes from ignoring the movement perpendicular to the film. We add all the distances in quadrature (the angles between different distances being uncorrelated) to get the total expected distance from the centre after m rounds of charge diffusion and photon emission. We should note that the expectation value $\sqrt{\langle \Delta x_{light}^2 \rangle}$ is considerably higher than $\langle \Delta x_{light} \rangle \approx 5\mu$m, and is largely dependent on the high tail of the PL. Results for light emitted at only particular wavelengths show great disparity in counts required to go a given distance.

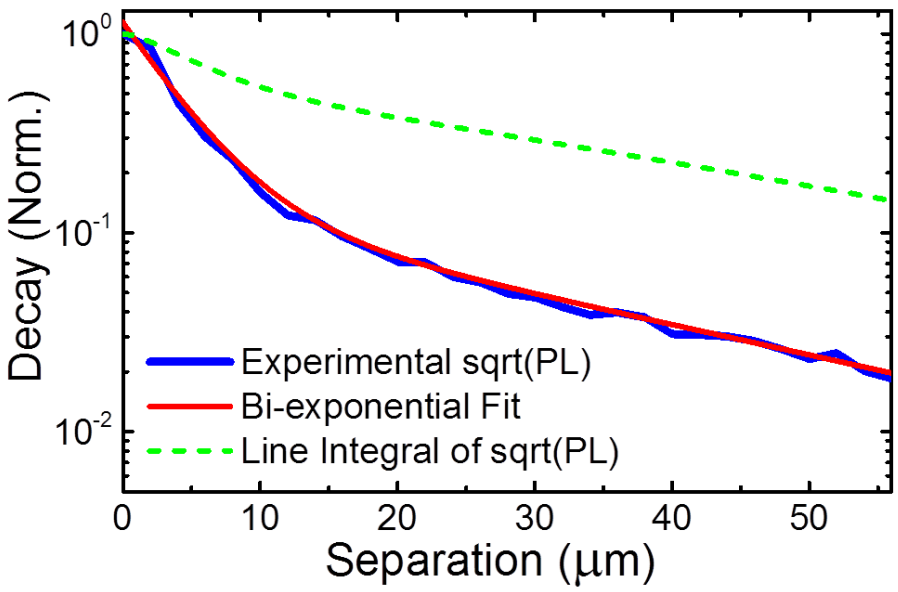

$$Corrected\ \sqrt{PL}\ (x) = \int_{-(length\ electrode)/2}^{(length\ electrode)/2} \left(a_1 e^{-(b_1 \cdot \sqrt{x^2+y^2})} + a_2 e^{-(b_2 \cdot \sqrt{x^2+y^2})}\right) dy$$

Fig. S19 Geometrical correction of the square root of the PL after integration along the electrode. The constants a1, b1, a2, b2 are extracted from a bi-exponential fit of the experimentally measured PL decay.